ADVANCED FUNCTIONAL MATERIALS
www.afm-journal.de

Flexible Triboelectric Nanogenerator Arrays for Energy Harvesting and Direct Current Output via Solid-Liquid-Gas Interfaces Involving Liquid Metals

Jiangtao Guo, Liangfei Duan, Wen Yang, Qin Wang, Xiyun Feng, Yunbo Zhang, Yong Zhang, Zhong Lin Wang, and Peizhi Yang**

Triboelectric nanogenerators (TENGs) efficiently convert mechanical energy into electricity, offering unique advantages for powering wearable electronics. Key objectives for wearable TENGs include flexibility, and high power density output. Liquid metals (LMs) are emerging as a category of functional materials with both metallic and liquid properties at room temperature, which opens up broader opportunities for TENG applications. Herein, a concept is proposed for constructing a fully flexible triboelectric nanogenerator array for mechanical energy harvesting by using LMs. The LMs layers are embedded in a porous polytetrafluoroethylene (p-PTFE) film, resulting in a series of parallel friction interface arrays. The strong electronegativity of PTFE and the high electronic activity of liquid metals are explored, and the interface at the solid-liquid-gas three-phase junction is constructed to facilitate the energy conversion. Using mechanical triggering, the direct current pulse is generated and amplified at the solid-liquid interface, resulting in an open-circuit voltage (V_{oc}) of 1080 V and a power density (P_{max}) of 12.44 W m^{-2}. Furthermore, V_{oc} generated by the device in the contact-separation mode amounted to 1690 V under ultrasonic (40 kHz) excitation. Consequently, this finding is anticipated to offer new opportunities in applications such as flexible electronics, mechanical energy conversion, and human-machine interaction interfaces.

1. Introduction

Liquid metals (LMs) represent an emerging class of soft matter systems within printable circuit,[1] characterized by their diverse functionalities, including stretchable electronics,[2] transfer liquids,[3] soft robotics,[4] and interactive computing capabilities.[5] The primary function of the LM-based elastomer technology is to facilitate the generation of information and energy through the conversion of mechanical energy into electrical energy.[6] Several potential solutions exist for achieving the efficient conversion of mechanical energy to electrical energy, such as elastomer generators based on the principle of the electric double layer (EDL)[7] and electrochemical generators based on the principle of redox.[8] The efforts to enhance these flexible power sources mainly focus on improving the power-to-mass ratio and power density. However, both EDL generators and elastomeric generators have their open-circuit voltage and short-circuit current dependent on the materials of the dielectric elastomer and device structure, and the open-circuit voltage and short-circuit current of elastomeric double-layer generators are contingent upon the materials utilized and the structural design of the dielectric elastomer.[9–11]

This poses requirements on the flexibility of such generators, as energy harvesting devices based on the EDL capacitors need sufficient deformation to cause changes in the quantity of electric charge. According to the capacitor equation $C = \Delta Q/\Delta t$, the charge quantity is intrinsically linked to the rate of change in capacitance.[12,13] Consequently, while this strain mechanism can accommodate the flexibility and elasticity of human skin and limbs, as well as facilitate discrete mechanical energy collection and utilization, its overall adaptability remains constrained. Furthermore, in the aforementioned flexible power generation devices, the design of a flexible and stretchable system is an essential objective. LMs have been extensively utilized as a flexible electrode; however, there are still several limitations in the current work.[14–17] First, the selection of a functionalized LMs conductive layer, typically utilized within an LMs/polymer composite system, may result in a reduction of intrinsic conductivity. Second, to prevent short circuit, an encapsulation layer of dielectric elastomer or a barrier layer of the electrochemical cell must be designed for the bulk material of LMs. Third, fluidity

---

J. Guo, L. Duan, W. Yang, Q. Wang, X. Feng, Y. Zhang, P. Yang
School of Energy and Environment Science
College of Chemistry and Chemical Engineering
Yunnan Normal University
Kunming 650500, China
E-mail: liangfeiduan@ynnu.edu.com; pzhyang@hotmail.com

Y. Zhang
Department of Electrical & Computer Engineering
University of North Carolina at Charlotte
Charlotte 28223, USA

Z. L. Wang
Beijing Institute of Nanoenergy and Nanoscience
Chinese Academy of Sciences
Beijing 101400, China

The ORCID identification number(s) for the author(s) of this article can be found under https://doi.org/10.1002/adfm.202510233

DOI: 10.1002/adfm.202510233

© 2025 Wiley-VCH GmbH

and adhesiveness of LMs as a liquid electrode make it susceptible to leakage. Finally, effective charge separation usually requires larger stress-deformation of the dielectric layer/electrode or contact separation. Besides, for the liquid metal/porous membrane composite interface, the high porosity facilitates the embedding of liquid metal into the fibrous pore structure, thereby forming spatial conductive channels. This is critical for ensuring the stability and high conductivity of the flexible circuit. Additionally, for the triboelectric properties of the porous dielectric materials,[18] the higher dielectric constant and the larger porosity of the fibers can form a highly porous network structure.[19] The large surface area to volume ratio of this structure will enhance the triboelectric performance of the device.

In this work, inspired by previous research,[20] we aimed to utilize LMs in combination with porous dielectric layers to create an elastomer film with an electric double-layer structure incorporating solid and liquid phases. This innovative approach enables the development of a flexible energy-harvesting device. In this study, we propose a triboelectronic-ion interface coupling mechanism at the solid-liquid-gas interface through the integrated synergy of triboelectricity and LMs elastomers. As a result, we achieve high performance of LMs triboelectronics with direct current - high voltage. The solid-liquid-gas interface formed by the room-temperature liquid metal elastomer resembles a resonant cavity, akin to a series of capacitors created by the LM layer interface. The presence of the porous dielectric layer/air gap and porous dielectric layer/LM embedded layer leads to a spatial charge distribution, with coupling between frictional charges and ion charges. When subjected to an external field, under the influence of the electric field, triboelectric electrons traverse through the porous dielectric layer while directed ion migration occurs due to the charge of LMs, thereby establishing a closed direct current circuit. This mechanism unifies the solid-liquid triboelectronics and triboelectric-ionics synergy effects in the LMs system, offering potential for novel flexible electronic devices integrated with energy-information systems.

2. Results and Discussion

2.1. Power Generation Mechanism of Room Temperature LM-TENG

This study presents a novel concept of a room temperature LM-TENG (RTLMs-TENG), consisting of insulating porous PTFE (p-PTFE) and LM thin layers as an active assembly, for a direct current (DC) generator. As shown in **Figure** 1ai-iii the RTLM-TENG structure of the porous PTFE/LM thin layer is achieved by printing the LMs on the rear side of the porous PTFE layer. This results in a front surface with a porous structure and a continuous conductive coating on the backside while maintaining flexibility of the porous membrane throughout. Specifically, we subjected the back side of the PTFE where the LM layer were printed to plasma treatment in order to enhance the wettability of LM on the p-PTFE and overcome its surface tension (refer to Videos S1 and S2, Supporting Information). By improving surface wettability, we successfully achieved a continuous and large-area coating of LM on the porous PTFE substrate (Figure S1a,b, Supporting Information). The LM material utilized was an eutectic GaInSn (eGaInSn) mixed with Cu particles, and the incorporation of Cu particles further enhanced the wettability of the LMs.[21] After plasma treatment, the PTFE surface exhibits excellent adhesion performance with metal droplets. As shown in the figure, the droplets continuously inject to form a continuous wetting layer, while the porous PTFE surface and the liquid droplets before plasma treatment are in a non-wetting state (Figure S1c–e, Supporting Information).

The p-PTFE/LM layered structure derived from the aforementioned steps exhibits array properties. First and foremost, microscopically, the portion where the LM clusters are embedded in the bottom of the p-PTFE can be equivalently treated as mutually parallel planar electrodes, connecting each micro-pore channel. Despite the random distribution of such pores, this model can be simplified as having a sufficient number of idealized pore structures within the effective area of each unit. Consequently, they can be regarded as micro-capacitors distributed in parallel. Therefore, the open-circuit voltage at points on the same plane is identical, resulting in $V_0 = V_1 \ldots = Vn$ (as depicted in Figure 1bi).

The spatial arrangement of the porous framework and the thin layer of the LM leads to the formation of a continuous three-phase interface consisting of solid, liquid, and gas phases, which is established by the ionic charges at the p-PTEF/LM interface and the spatial triboelectric charges (as depicted in Figure 1bii-iii). As depicted in Figure 1biv, the overall structure consists of a flat PTFE layer (encapsulation layer)/silver electrode/p-PTFE layer/liquid metal layer (also as the bottom electrode). The LMs of the scraped LMs/ porous PTFE layer is turned down and used as the bottom electrode, then the silver electrode is set on the front side of the porous PTFE layer, and finally a flat PTFE layer covers the silver electrode to serve as the encapsulation layer. This structure is similar to the discharge unit of the bioelectric system of electric-eel, and the discharge channels can form a parallel structure array to generate electrical output (as depicted in Figure 1bv). Another merit of this structure with the LMs embedded in the thin layer lies in that it can effectively prevent the leakage of the LMs, benefiting from the anchoring effect of the solid-liquid-gas three-phase interface,[22,23] thereby ensuring the overall flexibility and pliability of the device (Video S3, Supporting Information).

Consequently, triboelectricity charges on the gas/solid interface and ionic charges on the solid/liquid interface can be respectively extracted, creating an interface where frictional electrons and ions collaborate through division of labor.[24,25] The liquid phase embedding structure of the forwardly placed LMs/porous PTFE and the optical images of the flexible macroscopic LMs printed layer can be observed through the cross-sectional SEM images. Moreover, the EDS mapping results corresponding to different elements can clearly reveal the typical layered structure of the porous PTFE with F element and Ga, In, Sn, and Cu (Figure 1c).

The power generation mechanism is depicted in Figure S2 (Supporting Information). First, the gas/solid interface and the solid/liquid/gas interface form a continuous distribution boundary between the three phases (solid-liquid-gas). Due to the strong electric field induction provided by the PTFE dielectric layer, a relatively high charge density is induced at the solid-liquid interface (Figure S2i, Supporting Information).[26] Second, when the elastic interface undergoes deformation due to an external force, the polarization of the negatively charged PTFE will generate

© 2025 Wiley-VCH GmbH

16163028, 0, Downloaded from https://advanced.onlinelibrary.wiley.com/doi/10.1002/adfm.202510233 by University Of North Carolina, Wiley Online Library on [22/07/2025]. See the Terms and Conditions (https://onlinelibrary.wiley.com/terms-and-conditions) on Wiley Online Library for rules of use; OA articles are governed by the applicable Creative Commons License

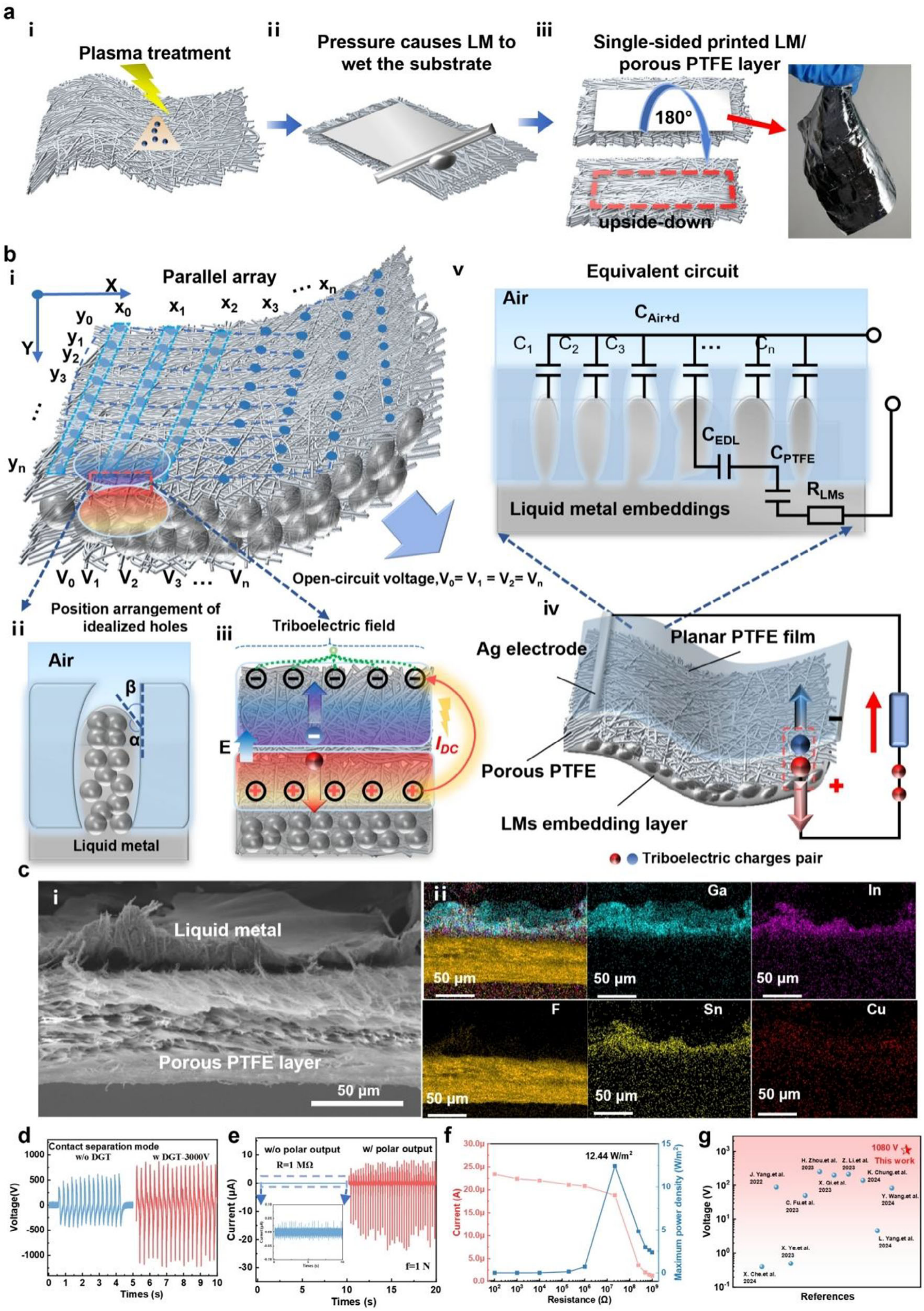

Figure 1. a) Schematic diagram of the process of preparing the porous PTFE layer by plasma treatment and scraping coating. b) The concept and interface diagram of the flexible porous PTFE/LMs layer array, the structural diagram of LMs-TENG and the equivalent circuit. c) SEM image and EDS energy spectrum of the LMs/porous PTFE cross-section. d) The V_{oc} of the device with/without a series GDT switch. e) The I_{sc} of non-polar/polar output mode. f) The load power curve of the generator. g) The recently reported voltage records based on liquid metal flexible generators.

© 2025 Wiley-VCH GmbH

16163028, 0, Downloaded from https://advanced.onlinelibrary.wiley.com/doi/10.1002/adfm.202510233 by University Of North Carolina, Wiley Online Library on [22/07/2025]. See the Terms and Conditions (https://onlinelibrary.wiley.com/terms-and-conditions) on Wiley Online Library for rules of use; OA articles are governed by the applicable Creative Commons License

more frictional charges on the polymer fibers of the porous PTFE, thereby enhancing the charge density at the solid-liquid interface (Figure S2ii, Supporting Information). Third, when the electric field at the solid-liquid-gas interface is sufficiently strong, charge separation will take place. Driven by an internal electric field, the frictional electrons mainly migrate upward from the LMs embedded layer/porous PTFE air gap, while the positive charges, namely the cations distributed in the liquid metal, migrate in the opposite direction. As a result, a current is generated in the equivalent circuit formed by the entire interface (Figure S2iii, Supporting Information). Finally, owing to the elastic restoring force of the multiphase interface, the LMs/embedded layer is equivalent to the liquid film plane generating a contracting liquid phase pressure. At this point, a relatively small reverse current is manifested, which is caused by the non-equilibrium charge at the boundary of the electrical double layer (Figure S2iv, Supporting Information).

Compared to recently reported droplet-based transistor-like structures,[27,28] the current output in our system is generated through a circuit consisting of the gate voltage, source, and drain at the solid-liquid interface. However, in this circuit, electrons do not directly pass through the dielectric layer and the output remains in an AC mode (Figure S3a, Supporting Information). The intensity of the DC output in this paper is determined by the TENG structures and interfacial electric fields. However, traditional elastomeric generator structures are primarily influenced by electrostatic induction or EDL charges, which necessitates a continuous process of strain elasticity and charge recovery during deformation restoration. This leads to a longer charge recovery time and impacts its output performance (Figure S3b, Supporting Information).

Therefore, it is noteworthy that certain porous dielectric layers possessing insulating properties can effectively capture and transfer charges under specific conditions, suggesting their potential role as barriers in air environments. Within this solid/gas/solid continuous network structure, ions within the LMs thin layer embedded in minute air gaps are adsorbed at the interface of the porous matrix. This implies that instead of relying on significant deformation observed in conventional bulk LMs, for charge extraction from the elastomeric shell can be achieved through continuous variations in the three-phase contact line at the solid-liquid-gas interface.[29] In the contact-separation mode, the device in series with the (gas discharge tube) GDT switch can generate an average maximum peak voltage of 1080 V. By contrast, for the device not in series with the GDT switch, the average peak output voltage reaches 374 V (Figure 1d). Meanwhile, to verify the blocking characteristic of the built-in electric field within the porous PTFE interface, we hypothesized that the output mode through the bottom electrode and the upper electrode is the polar output mode. The loop formed by directly connecting the bottom electrode of the device to a 1 MΩ resistive load was taken as the control group, and the measured output current (0.036 μA) was regarded as the non-polar output mode. It can be observed that the polar output mode has been elevated by three orders of magnitude (Figure 1e). Finally, we tested its output power, and it can be observed that the power density reaches 12.44 W m^{-2} (Figure 1f). A comparison was made with the output voltages of the recently reported flexible generators based on liquid metal, as depicted in Figure 1g.[30–37] In this work, a landmark highest open-circuit voltage was attained, with the output voltage of 1080 V in the contact-separation mode, which higher than the recently reported output of TENGs based on LMs in either AC or DC mode.

2.2. Mechanism of Charge Transport at Multiphase Interfaces

Logically, the electron capture/emission of LMs typically occurs in an electrochemical/liquid environment. Whereas, the phenomenon of charge conduction across air/solid/liquid media has received little attention. In order to elucidate the conduction mechanism of triboelectric charges, we investigated the electronic states at the solid-liquid interface and the solid-liquid-gas three-phase interface, specifically focusing on the interface between PTFE and LMs. To test the charge conduction between the upper electrode/porous PTFE and the LMs-porous PTFE/lower electrode through mechanical contact and separation, we devised an experimental setup as illustrated in **Figure 2a**). In scenario one, a light contact force was applied to the PTFE surface followed by rapid or delayed separation. In scenario two, a greater contact force was exerted on the PTFE surface before undergoing rapid or delayed separation.

Due to its insulating properties, when subjected to the lower pressure stimuli, the porous PTFE membrane generates a triboelectric field that is inadequate for exciting and migrating triboelectric electrons within the gas-solid structure. This behavior is similar to the charge separation process observed in the traditional single-electrode electrostatic induction mode (as shown in Figure 2b). The resistance between the two electrodes ranges from 100 to 300 GΩ, thus maintaining an open-circuit state. Unlike the conventional elastomer interfaces, the charge of this device is not primarily determined by the volumetric deformation of the LMs. A distinct solid-liquid-gas multiphase interface forms an internally biased triboelectric field, as illustrated in Figure 2c. In its initial state, it represents a static charge distribution; subsequently, when subjected to an external mechanical trigger, a sufficiently strong electric field can be induced between the electrode and the solid-liquid-gas interface until reaching maximum compression state.

Consequently, charge separation occurs within the internal charge migration channels and at the LMs interface in this mechanism.[38] The triboelectric electrons predominantly migrate from porous PTFE while opposite-polarity cationic charges achieve charge separation at the EDL interface, thereby completing a power generation cycle. Moreover, due to substantial effective contact area at the solid-liquid interface, there exists relatively high EDL charge density associated with the porosity of porous PTFE. Therefore, the application of external stress results in non-equilibrium electric field formation at the three-phase solid-liquid-gas interface, leading to subsequent pronounced output.

For the sake of simplicity, we define the mode 1 as having the upper electrode as the negative output and the bottom electrode as the positive output, while the mode 2 refers to reversing the positive and negative output terminals. Subsequently, we conducted current tests for these two output modes. It is evident from Figure 2d that mode 1 exhibits a distinct current output, thereby indicating the direction of the electric field interface.

© 2025 Wiley-VCH GmbH

16163028, 0, Downloaded from https://advanced.onlinelibrary.wiley.com/doi/10.1002/adfm.202510233 by University Of North Carolina, Wiley Online Library on [22/07/2025]. See the Terms and Conditions (https://onlinelibrary.wiley.com/terms-and-conditions) on Wiley Online Library for rules of use; OA articles are governed by the applicable Creative Commons License

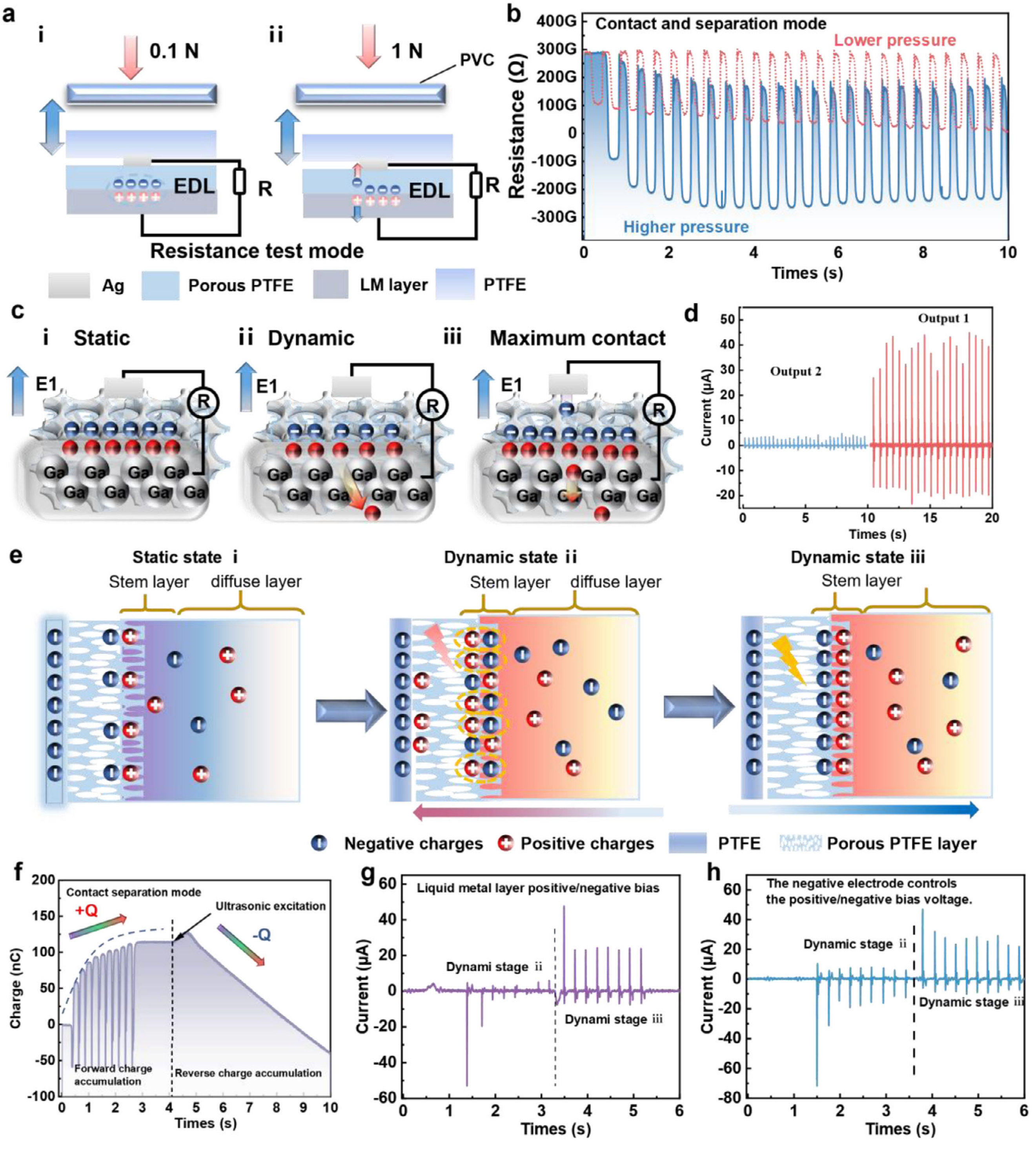

Figure 2. a) The DC output circuit diagram. b) The corresponding resistance curve under different pressure conditions. c) Mechanism diagram of the electric field at the interface of the layered LMs embedded in the porous PTFE. d) Current in different output modes. e) The solid-liquid double electric layer model of the multiphase interfaces. f) Charge transfer curves under the contact-separation mode and ultrasonic mode. g) The output current of injecting positive charges into the LMs layer. h) The output current of injecting negative charges into the negative electrode.

© 2025 Wiley-VCH GmbH

16163028, 0, Downloaded from https://advanced.onlinelibrary.wiley.com/doi/10.1002/adfm.202510233 by University Of North Carolina, Wiley Online Library on [22/07/2025]. See the Terms and Conditions (https://onlinelibrary.wiley.com/terms-and-conditions) on Wiley Online Library for rules of use; OA articles are governed by the applicable Creative Commons License

Similarly, we also tested the conductivity between the electrodes under these two modes, as shown in Figure S4 (Supporting Information), the resistance range of the device in the contact separation condition under the output mode 1 is still on the order of 3×10^{11} Ω, while the resistance remains open under the output mode 2, which also indicates that the working mode polarity opposite to the built-in electric field cannot drive electrons to conduct across the multiphase interface.

One advantage of the charge partitioning collaborative interface is that, unlike the traditional contact-separation modes, the excitation mode for charges is related to field effect.[39] This direct current mode can be viewed as a parallel circuit on the interface, and thus its output is proportional to the contact area. To demonstrate this charge output and frequency response limits, we designed a system consisting of an ultrasonic generator and transducer as an external field excitation source without altering the original circuit connection method. We directly tested its DC output performance using front-facing ultrasound in a sweep mode (Figure S5, Supporting Information), and ultrasound is stimulated on the front side of the RTLMs-TENG.

In order to achieve effective input of energy in the contact-separation and ultrasonic modes, we also examined the situation where the TENG was placed vertically on the upper surface of the ultrasonic generator. The voltage and current exhibit periodic signal patterns related to the ultrasound sweep mode with a voltage range of −70V to +20V and a current of 0.8 μA. It is evident that as the ultrasonic power increases, the rate of charge transfer induced by ultrasonic waves also rises, resembling an acoustic resonator. However, this increase is constrained. At 30W, the maximum charge transfer rate can reach up to 589 nC s^{-1} (Figure S6, Supporting Information).

The model of contact electrification - double electric layer interface proposed recently by Wang et al.[40,41] can explain the charge distribution characteristics of the multiphase interface and can be divided into three stages. In stage 1, the double electric layer distribution of the LMs embedded layer caused by the initial charge of the PTFE dielectric layer is shown in Figure 2e. At this point, the charge density is relatively low. Then in stage 2, with the contact electrification mechanism caused by mechanical energy stimulation or continuous excitation of the external field, it will lead to an increase in the charge density of the multiphase interface. At this time, we can change the polarity of the LMs double electric layer charge through external charge injection. Additional positive charges will be temporarily stored near the surface of the porous PTFE, and correspondingly, the negative charges distributed in the diffusion layer of the LMs are more than the positive charges. Finally, in the third stage, when we continue to inject negative charges, the LMs double electric layer charge restores its original polarity, and at this time, there are more positive charges distributed in the diffusion layer.

In order to validate the aforementioned mechanism, two distinct modes were employed to test the characteristics of charge transfer. First, the contact-separation mode (2 Hz) was utilized, followed by ultrasonic excitation applied to the backside of the device after a delay of 2 s. The results, depicted in Figure 2f, demonstrate that with an increasing number of contact-separation events, the charge exhibits a stepwise upward trend indicating significant charge accumulation at the interface. We define this process as the charging stage and represent it as +Q, consistent with previous observations.

Moreover, activation of ultrasound initiates a reversal in the "charging" curve with a representation of -Q for charges. This suggests different accumulation patterns on both sides of the interface electric field emerge. Due to the abundance of cations, free radicals, and frictional charges present on the solid-liquid interface of LMs compared to mainly static frictional charges on the gas-solid interface side, the continuous accumulation of frictional electrons occurs during the contact-separation at the porous interfaces.[42] Each contact-separation event leads to an increase in the charge density accordingly. Similarly, it can be hypothesized that the ion charge EDL oscillation at the solid-liquid interfaces generates continuous charging behavior where charges are stored, whereas the output current, when such an ultrasonic field is incident from the back surface of the generator, still demonstrates a DC characteristic, as depicted in Figure S7 (Supporting Information). The transfer charges through three consecutive cycling periods of the continuous ultrasonic and contact-separation modes exhibit a stable trend (Figure S8, Supporting Information). The direction of the electric field at this interface will influence the charge accumulation tendency produced by the ultrasonic field in the opposite direction. The charge accumulation tendency can be observed from the charge curves (Figure S9a,b, Supporting Information) when the ultrasonic field is incident from the front.

Furthermore, we have also designed an experiment for charge injection using an electrostatic bias source. Inspired by the separation and recombination mechanism of photovoltaic carriers, we have explored the influence of the initial charge excitation on the inherent electric field of the solid-liquid-gas multiphase interfaces. An electrostatic gun was employed to control the positive and negative biases and was connected to the LMs layer as well as the positive electrode of the electrometer. The cyclic output indicated that the pulses of positive and negative currents could serve as the charge source (Figure S10a, Supporting Information). Subsequently, a negative charge injection excitation was applied to the device. As depicted in Figure S10b (Supporting Information), the output current changed from negative to positive, and the current amplitude exhibited a trend of gradual recovery.

To illustrate the impact of additional negative charges on the EDL distribution at the solid-liquid interface, we tested the output current trend of the contact separation while injecting negative charges simultaneously. As shown in Figure 2g, the output current rapidly changed from negative to positive, which was attributed to the diffusion layer charge of the non-equilibrium charge output caused by the instantaneous negative electric field impact. With the polarity reversal, the output current transformed into a positive pulse. The universality of a similar mechanism was also demonstrated when the negative electrode was used as the charge injection window. Due to the blocking effect of the multiphase interface electric field, the injected charges were captured and stored in the shallow layer of the porous PTFE. At this solid-liquid interface, ions of the opposite polarity were attracted, thus enabling the negative current to maintain a certain output. Subsequently, the current transformed into a positive pulse again as the external electric field changed (Figure 2h).

Theoretically, previous LMs elastomers typically exhibited only one type of charge property, overall having the property of a

© 2025 Wiley-VCH GmbH

16163028, 0, Downloaded from https://advanced.onlinelibrary.wiley.com/doi/10.1002/adfm.202510233 by University Of North Carolina, Wiley Online Library on [22/07/2025]. See the Terms and Conditions (https://onlinelibrary.wiley.com/terms-and-conditions) on Wiley Online Library for rules of use; OA articles are governed by the applicable Creative Commons License

metal conductor, but usually enveloped by insulating dielectric elastomers; thus, the charge of the ionic interface EDL was disregarded.[43] Nevertheless, porous PTFE is a material with a strong charge-trapping capability. Therefore, the electrostatic field of its porous structure plays a role in regulating the EDL charge of the LMs.

2.3. The Charge Accumulation Mechanism on Multiphase Interfaces

The initial state of the multiphase interface in the elastic structure can be defined as a non-wetting state between the gas-solid phase and the liquid phase (**Figure** 3a). As the external pressure is applied to the interface, the porous structure gradually becomes wetted by the LMs layer. A balance is achieved with the LMs layer due to capillary forces within the porous structure and the blocking action of the air gaps. At this stage, a stable distribution occurs where the LMs is embedded in the porous framework. Consequently, a continuous distribution of solid-liquid-gas three-phase lines forms at the multiphase interface. The symmetric distribution of double-layer charges

To demonstrate the universality of electron accumulation at the solid-liquid-gas interfaces, we devised an experimental setup to validate the liquid-blocking/charge-accumulation properties inherent in such interfaces. By utilizing a frozen LMs cylinder as a solid-state medium, its adjustable positioning facilitated a controlled movement of a molten LMs droplet along its length. As depicted in Figure 3b, when the droplet remains stationary on a porous PTFE surface, it assumes a spherical shape. Upon contact with the PTFE surface, the droplet undergoes further compression, resulting in increased contact area; subsequently detaching from the PTFE surface allows for elastic deformation recovery. The continuous process of contact and separation is illustrated in Video S4 (Supporting Information). Subsequently, corresponding amplification signals for single voltage charge (Figure 3d), voltage accumulation (Figure 3e), and charge accumulation (Figure 3f) respectively exhibit an increasing trend, indicative of charge transfer and accumulation between LMs and solid polymer surfaces. A continuous process was documented in the high-speed photography (Video S5 and Figure S11a, Supporting Information). Subsequently, as the LMs droplet further melted, the solid-liquid contact area increased. Due to the gravitational force of the droplet, the droplet separated from the non-melted solid portion and was thus adsorbed onto the PTFE surface. Nevertheless, with the persistence of the contact and separation process, the voltage and charge signals continued to accumulate and increase (Figure S11b,c, Supporting Information).

Furthermore, it was observed that the three porous PTFE membranes utilized in this experiment exhibited distinct microstructural parameters, which is characterized by SEM as shown in Figure 3g–i. The PTFE porous membrane possesses the characteristic of randomly distributed micro-nano multistage structure. The PTFE porous membranes with different parameters have similar pore size structural characteristics. Specifically, the pore characteristics of Sample 01 are larger, while the pores of Sample 02 and Sample 03 membranes decrease successively. Owing to the generally non-wetting nature of liquid metals, for example, eGaInSn and Hg have similar properties, and they are not wet by common solid surfaces (with a contact angle greater than 90°). Therefore, based on the results of the mercury intrusion test, by measuring the amount of mercury that enters the pores under different external pressures, the pore volume corresponding to the pore size can be known. The pore size distributions of the three PTFE porous membranes are presented in Figure 3j–l. It can be clearly discerned by the distribution characteristics of their main pore structures. Each peak represents the volume of the corresponding largest pore. Furthermore, the porosities of the porous membranes are obtained in sequence as 79.5%, 72.6%, and 61.6%, respectively.

Considering that the pressure range of the mercury intrusion test is 0.10–61 000.00 psia, this interval covers the maximum extreme pressure that the PTFE porous membrane might withstand. Therefore, through increasing pressure in the mercury intrusion and extrusion curve, the intrudable pore size becomes smaller and smaller (Figure S12a–c, Supporting Information),[44] as well as the proportion of pore length corresponding to pore size., which is obtained by dividing the volume by the pore size (Figure S12d–f, Supporting Information). The average pore size within the porous framework was measured at ≈1 µm, facilitating the formation of an interconnected network for LMs penetration. Consequently, for the samples in this experiment, the interplays among the solid-liquid-gas multiphase interface, capillary forces, and surface tension will generate a balancing force. The LMs are anchored in the liquid phase portion of the PTFE porous structure and the non-wetted regions within the PTFE porous structure.

To demonstrate that frictional charge accumulation occurs universally between LMs and porous interfaces, we also separately tested the charge transfer between LMs filled porous conductive polyurethane foam (PU) foam and porous PTFE under sustained pressure, as shown in Figure S13a,b (Supporting Information). It can be seen that the transferred charge quantity shows a gradually accumulating growth trend (Figure S13c,d, Supporting Information), which may be due to the accumulation of ions at the porous interface, showing a charge trend similar to the DC characteristic of the device interface in this experiment.[45] Similarly, the copper content in the LMs also affects the output performance of the device. It is found that as the copper content increases, both the open-circuit voltage and short-circuit current show a decreasing trend. This might be due to the gradual solidification of the liquid metal as the solid component increases. Therefore, the interfacial interaction force between the LMs and the porous PTFE decreases, leading to a decline in output performance (Figure S13e,f, Supporting Information).

Consequently, a stable liquid thin film interface is formed with interstitial gaps within the porous framework to establish a distribution of solid-liquid-gas continuous phase (Figure S14, Supporting Information). The cross-section of the room-temperature LMs elastomer is divided into liquid thin layers and porous frameworks, wherein the LMs interface resembles an elastic membrane that exhibits similar elastic-recovery properties to a rigid porous membrane at the solid-liquid-gas interface. The solid-liquid-gas coupling interface has interface elasticity, so the interface elasticity and the triboelectric field effect work together. Therefore, we investigated the influence of the encapsulation layer PTFE and the porous PTFE dielectric layer on the output performance of the device, as shown in Figure 3m,n. It

© 2025 Wiley-VCH GmbH

16163028, 0, Downloaded from https://advanced.onlinelibrary.wiley.com/doi/10.1002/adfm.202510233 by University Of North Carolina, Wiley Online Library on [22/07/2025]. See the Terms and Conditions (https://onlinelibrary.wiley.com/terms-and-conditions) on Wiley Online Library for rules of use; OA articles are governed by the applicable Creative Commons License

16163028, 0, Downloaded from https://advanced.onlinelibrary.wiley.com/doi/10.1002/adfm.202510233 by University Of North Carolina, Wiley Online Library on [22/07/2025]. See the Terms and Conditions (https://onlinelibrary.wiley.com/terms-and-conditions) on Wiley Online Library for rules of use; OA articles are governed by the applicable Creative Commons License

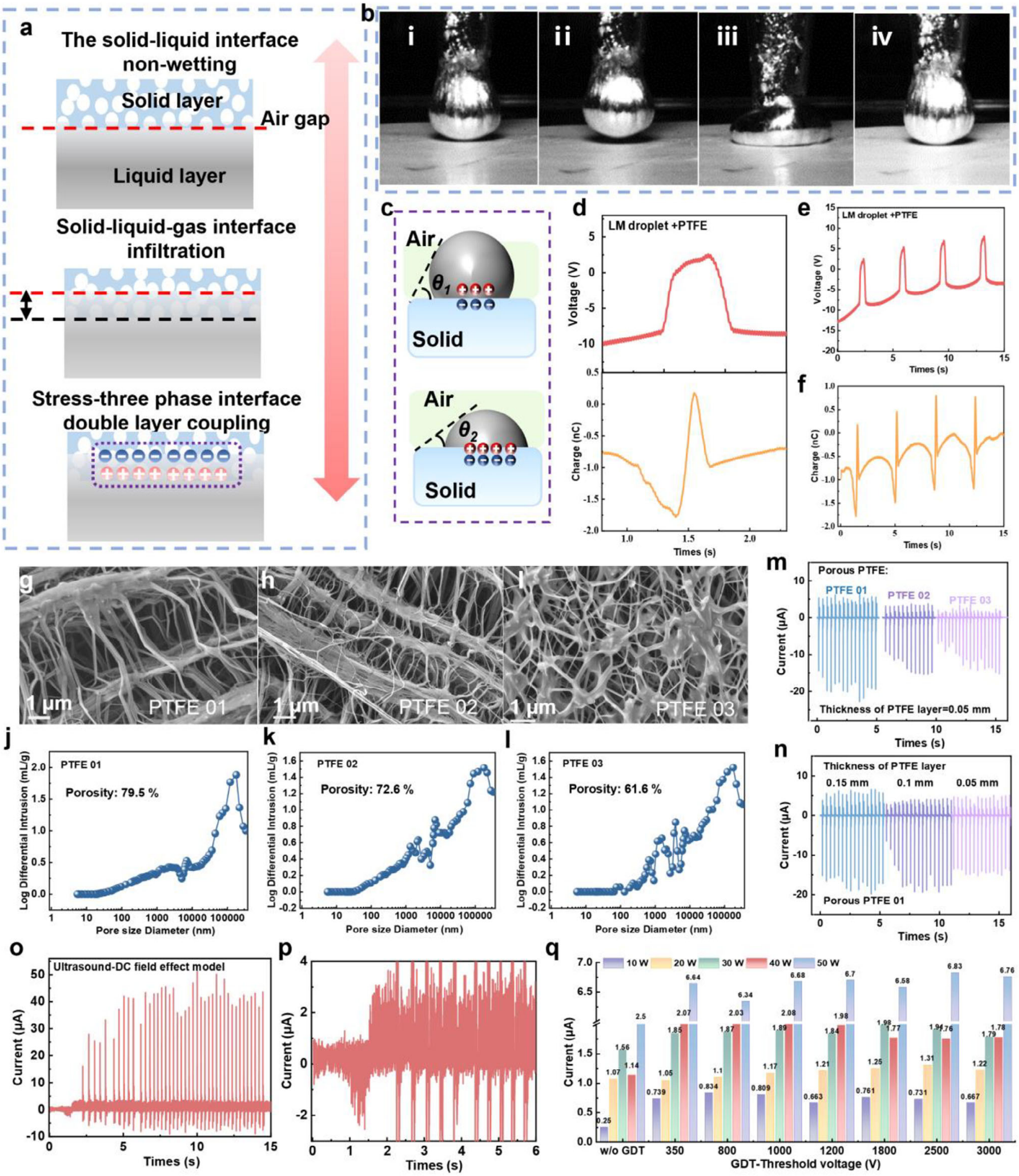

Figure 3. a) Porous PTFE layer and LMs embedded layer with solid-liquid-gas multiphase interface structure. b) Dynamic test of LMs droplets and c) the wetting mechanism at the solid-liquid interface. d) The amplified V_{oc}, I_{sc} signals and e) continuous V_{oc}, f) Q_{sc} signals when LMs droplets contact and separate from the porous PTFE surface. g–i) SEM images and j–l) pore size distribution obtained from mercury intrusion tests for the porous PTFE membranes with different parameters. m) The output current of devices constructed with different porous PTFE membranes. n) The output current of devices with different PTFE encapsulation layers. o) The current and amplified signal of the device in a hybrid output of ultrasonic excitation and p) contact-separation mode. q) The electrical output performance of the device in series with the discharge switch.

can be discerned that the output currents of the devices based on the No. 01, No. 02, and No. 03 porous PTFE membranes decrease in sequence. Simultaneously, we also studied the impact of the PTFE encapsulation layer on the output current of the device based on the No. 01 porous PTFE membrane. It can be perceived that the output current decreases successively as the thickness of the PTFE encapsulation layer increases. The aforementioned trends suggest that the porosity of the porous PTFE dielectric layer might exert an influence on the built-in electric field at the solid-liquid-gas interface. The higher the porosity is, the more triboelectric charges are stored in the internal pores, thereby demonstrating a higher peak current intensity and thus playing a predominant role.

Subsequently, in order to further examine its elastomeric effect, we conducted tests on the output of the device under the simultaneous excitation of ultrasonic and contact-separation modes. First, as shown in Figure 3o, it starts in a static state and then ultrasonic excitation is initiated. The initial current is caused by the charge oscillation of the multiphase interface induced by ultrasound. The typical feature is that the current is initially reversed, which is due to the transient effect of ultrasound during the on and off states and the maximum amplitude of the current exceeds 2 µA. After stabilization, a continuous direct current output is generated. Then, we apply mechanical contact-separation pules on the RTLMs-TENG. It can be observed that the current continuously increases and reaches 40 µA (Figure 3o,p). This suggests that the electric field of this charge division and collaboration interface can effectively separate charges, generating a continuous direct current output whether under low-frequency or high-frequency conditions. This is distinct from the traditional contact-separation mode of the RTLMs-TENG, which must resort to precise sub-micron scale structure design to convert ultrasonic energy into electrical energy.[46,47] Finally, a circuit with a series-connected gas discharge tube (GDT) was designed to manage the output in the ultrasound-to-ultrasound mode, as depicted in Figure 3q. Under different output power ultrasonic modes, the device with the GDT in series exhibited an enhanced output with an increase in the conduction voltage, thereby effectively achieving energy management.

2.4. The Influence of Solid-Liquid Phase Change on the Interface Electric Field

For the solid-liquid-gas interface, the contact force under the same conditions was measured for its direct current (DC) at different temperature intervals, as depicted in **Figure** 4a. First, the RTLMs-TENG was cooled down to 0 °C and then continuously heated to 60 °C. This process was accomplished through a semiconductor temperature control platform to realize the continuous temperature variation of the device, and the surface temperature was detected throughout the entire process by a thermal imager. Therefore, to represent this internal electric field mechanism, it can be classified into three stages, In the first stage, at 0 °C (as indicated by thermal imaging of the actual surface temperature), the LMs is in the solid phase (Figure 4ai); in the second stage, as the temperature gradually rises from 0 °C to the room temperature of 25 °C, the LMs transitions into a solid-liquid mixed state and then to the liquid state at room temperature (Figure 4aii); in the third stage, it is in the fully liquid state, where the temperature reaches 50 °C (Figure 4aiii). Subsequently, the corresponding continuous charge and current outputs are also different. As shown in Figure 4b,c, the charge increases from 5 nC all the way to 80 nC. Simultaneously, the current is 10 µA at 0 °C, while it rises to ≈50 µA at 15 °C. This phenomenon of in situ current enhancement with the increase in temperature might suggest that the liquid metal embedded layer within the porous structure of the PTFE membrane has a greater effective solid-liquid contact area when in a completely liquid state, thereby generating a higher charge density and leading to a larger current output.[48,49]

In order to demonstrate the disparity between the LMs thin layer and the conventional bulk material state, thermal imaging was employed to characterize the LMs droplets, while a temperature control platform was utilized to regulate the temperature of these droplets deposited on the surface of the PTFE layer. As depicted in Figure 4d, a significant discrepancy in temperature was observed between the liquid droplets and the PTFE substrate. This phenomenon can be attributed to the extensive contact area that exists between air and LMs, resulting in a pronounced temperature gradient within its surrounding region constantly interfacing with PTFE. Continuous thermal imaging within the range from room temperature to high temperatures is presented in Figure S15 (Supporting Information). Consequently, this observation further validates the high thermal conductivity possessed by LMs. Similarly, in the vicinity of 0 °C, the core temperature also exhibits a temperature disparity with the surrounding temperature (Figure S16a, Supporting Information). We can infer that at this moment, the planar device has a relatively uniform core temperature and a faster heating rate due to the heat conduction effect of the part in contact with the air. Therefore, it can be determined that the overall thermal distribution difference is indeed caused by the solid-liquid phase transition and air heat conduction.[50,51] Subsequently, the thermal imaging features of the device at room temperature after further heating are shown in Figure 4e, where the high-temperature regions spread gradually from the center to the surroundings due to the LMs layer being in a liquid structure at this time, thus resulting in more uniform heat conduction. To expand the properties of this interface LMs phase transition, we designed a handwriting demonstration interface. Direct finger-point contact on the device surface would generate a continuous spatial matrix distribution of hot spots, as shown in Figure 4f.

Furthermore, the real-time output current can also reflect the trend of variation with temperature, as illustrated in Figure 4g. When the sample was rapidly restored from 0 °C to the room temperature of 15 °C, the output current increased from 0.5 to 50 µA, and the pressure conditions of this test were the same as before. During the 0–15 °C range, the peak current exhibited a rapid upward trend (Figure S16b, Supporting Information), and then remained relatively stable. To further affirm the transformation of the elastomer from rigidity to flexibility, we also compared the transfer charge trends of the samples under these two temperature conditions.

To detect the effective charge separation of the elastomer structure, we first inspected the output of the sample under ultrasonic excitation conditions, as depicted in Figure 4h. It can be observed that the slope of the charge curve shows a significant difference between 0 °C and 25 °C. It can be seen that due to the DC output

© 2025 Wiley-VCH GmbH

16163028, 0, Downloaded from https://advanced.onlinelibrary.wiley.com/doi/10.1002/adfm.202510233 by University Of North Carolina, Wiley Online Library on [22/07/2025]. See the Terms and Conditions (https://onlinelibrary.wiley.com/terms-and-conditions) on Wiley Online Library for rules of use; OA articles are governed by the applicable Creative Commons License

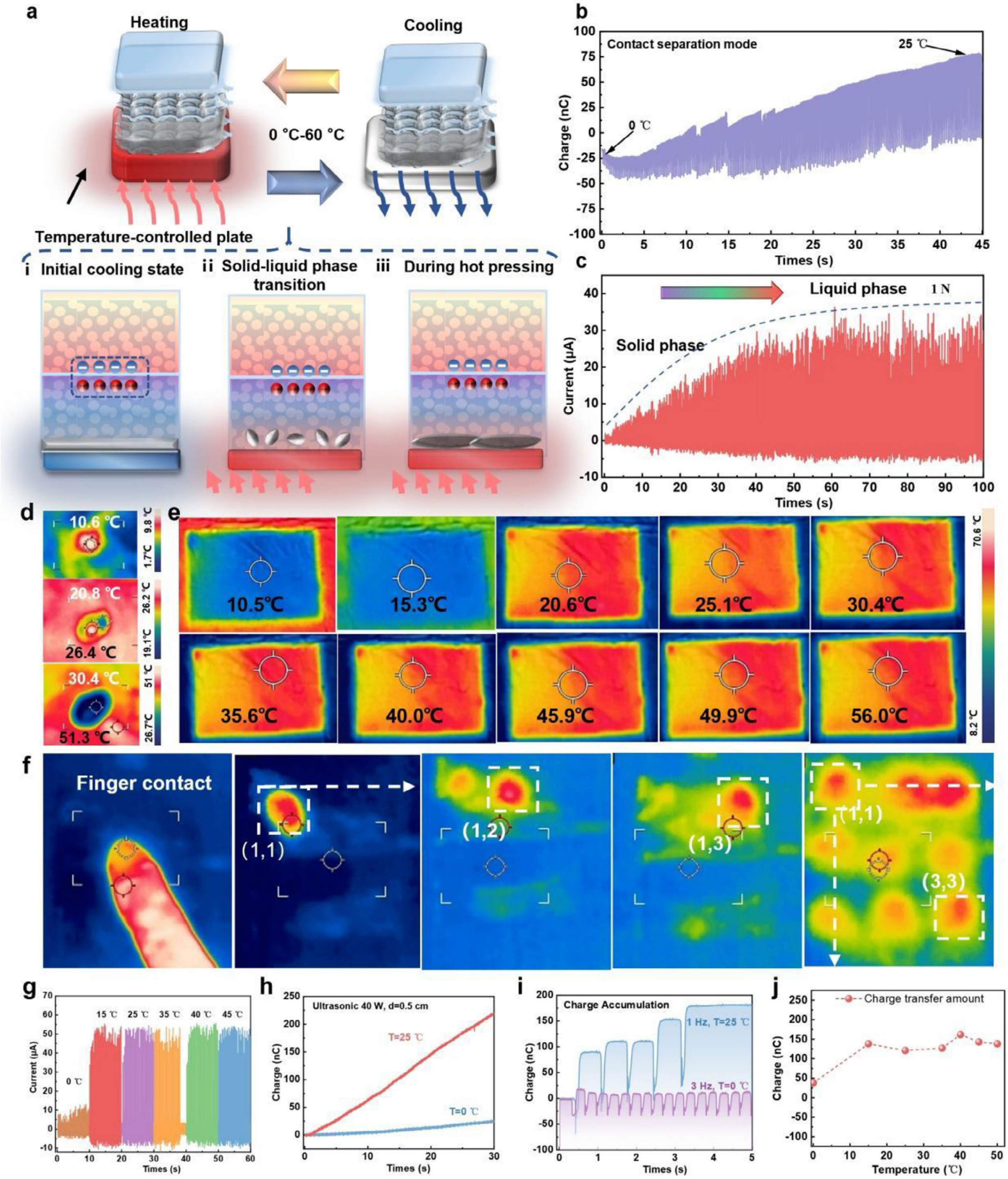

Figure 4. a) A schematic diagram of the device for controlling the solid-liquid phase transition of LMs. b) The impact of temperature on Q_{sc}. c) The effect of temperature on output current I_{sc}. d) Thermal imaging pictures of the LMs droplets/PTFE layer during continuous temperature variations. e) Continuous thermal imaging distribution of the device when heated from room temperature to high temperature. f) Thermal imaging distribution of writing with direct finger touch. g) Current output at different temperatures. h) Charge curves under ultrasonic excitation at 0 °C and 25 °C. i) Charge curves for contact-separation mode at 0 °C and 25 °C. j) Charge curves for contact-separation mode at different temperatures.

© 2025 Wiley-VCH GmbH

16163028, 0, Downloaded from https://advanced.onlinelibrary.wiley.com/doi/10.1002/adfm.202510233 by University Of North Carolina, Wiley Online Library on [22/07/2025]. See the Terms and Conditions (https://onlinelibrary.wiley.com/terms-and-conditions) on Wiley Online Library for rules of use; OA articles are governed by the applicable Creative Commons License

characteristic of RTLMs-TENG, at 25 °C, the charge continues to increase linearly with time, while at 0 °C, as a contrast, the charge shows a slow increase trend. This also reflects the state of the solid-liquid phase transition from flexibility to rigidity, and the increase in the accumulation amplitude is consistent with the results of our current measurement. Second, the charge in the contact-separation mode also verifies this trend. As depicted in Figure 4i, at 0 °C, the charge accumulation is nearly negligible and only exhibits a single charge transfer quantity. However, at 25 °C, the charge transfer quantity accumulates in a stepwise pattern, suggesting that with a higher temperature, the charge transfer quantity also presents an overall increasing trend (Figure 4j). The above results fully indicate that in the interface of the RTLMs-TENG, the solid-liquid phase transition of the LMs layer not only affects the distribution of electrons but also influences the overall elasticity and rigidity of the structure.[52]

Then we tested the energy output characteristics of the device and established an equivalent circuit as shown in **Figure 5a**. Due to its DC output characteristics, we can use a discharge switch as a charge pump in series to realize an automatic switching mechanism. When the voltage across the discharge switch reaches its on-state voltage, the loop will be connected, producing a brief discharge.[53] Then we added a capacitor in parallel to increase the current output. We then tested the power load characteristics in ultrasonic mode, as shown in Figure 5b. As the resistance increases, the current gradually decreases, and then the output power reaches its maximum value. And, the output currents of the contact-separation mode under a load of 1GΩ and the output currents of the contact-separation mode under ultrasonic excitation were tested, as shown in Figure 5c,d, respectively, which exhibit obvious coupling enhancement effects. The output currents of the two modes are higher than those of the single mode. At the same time, the output current of the device under a load of 1GΩ for the contact-separation mode can be seen to be caused by the enhancement of the charge density induced by the field effect (Figure S17a,b, Supporting Information). We propose an equivalent circuit to account for this field effect enhancement phenomenon. Assuming that the device resembles a charge source, in accordance with Ohm's law, $V_{total} = V_1 + V_2$, where V_1 is the voltage generated by the contact separation mode, V_2 is the voltage excited by the ultrasonic field, and V_{total} is the total voltage at the LMs interface. Thus, the additional excited electric field will be serially superimposed at the LMs interface, thereby manifesting as a higher open-circuit voltage.

To demonstrate this charge enhancement mechanism, we also investigated the transfer charge situation when the two modes were mixed, as shown in Figure 5e. With the increase of ultrasonic power, the charge transfer rate generally increases. It is worth noting that the coupling enhancement of the contact separation mode and the ultrasonic mode is indeed reflected in the higher charge transfer rate performance. The mixed output of different ultrasonic power and contact-separation modes is shown in Figure S18 (Supporting Information). The corresponding physical device and its enlarged structure are depicted in Figure 5f. The bracket used for fixing the device maintains a certain air gap from the ultrasonic transducer. In an actual demonstration case, the ultrasonic and contact-separation hybrid excitation mode is presented in Figure 5g, and it can even be triggered by directly patting with the hand. Pre-stress, such as tensile force, may influence the elastic behavior of the microstructural coupling interface. However, it exhibits excellent stability within the tensile force range of 1–5 N (Figure S19a,b, Supporting Information), until the ultimate tensile force leads to the failure of the main structure (Figure S19c, Supporting Information). Meanwhile, the oxide layer on the surface of the liquid metal has a self-passivation mechanism, showing good interface stability. The packaged devices were subjected to a continuous 7-day stability test, as shown in Figures S20, S21 (Supporting Information), indicating stable device performance. The performance of 10 devices was also tested and is shown in the Table S1 (Supporting Information).

Additionally, as a flexible wearable device, human comfort and conformability are also factors of interest. We conducted mechanical cycling tests on the device in a bent state, as shown in Figure S22 (Supporting Information), and bent the thin-film device into a circle to perform dynamic compression deformation tests (Figure S23, Supporting Information). It can be seen that it still has a significant output under mechanical bending and compression conditions. In Figure 5h, we compared the thermal imaging photos when the device was placed on the palm and wrist, indicating its certain heat management capability. Subsequently, we designed a demonstration function of continuous handwritten digit recognition (Figure 5i). The distribution of thermal imaging exhibits a distinct contour. The rapid response capability of the device based on the solid-liquid-phase transition was further demonstrated through the interactive demonstration interface triggered by hand patting. As shown in Figure 5j–m, they are the thermal imaging distributions of rapid finger point contact, one-finger trigger, two-finger trigger, and three-finger trigger, respectively. The corresponding voltage and charge signals are presented in Figure 5n–q. It can be observed that as the effective contact area between the hand and the device increases, the electrical output signal also increases, suggesting that it possesses certain potential for human-machine interaction and can be applied in self-driven human-machine interaction sensing and infrared recognition communication.

3. Conclusion

In this study, we report a TENG for energy harvesting based on room-temperature liquid metal. This approach entails the incorporation of a LMs layer comprising gallium, indium, tin, and copper within the porous dielectric layer of PTFE film on the reverse side, resulting in the formation of a multiphase distribution structure characterized by solid-liquid-gas interfaces. The hybrid energy harvesting characteristics of RTLMs-TENG and the performance enhancement through the coupling of ultrasonic and contact-separation modes were investigated. The generator is capable of generating an open-circuit voltage of up to 1080 V and a power density of 12.44 W m^{-2}. Finally, the human-machine interaction and wearable characteristics based on thermal imaging and electrical sensing outputs were presented, suggesting the potential application value of this device in future flexible self-powered wearable scenarios.

© 2025 Wiley-VCH GmbH

16163028, 0, Downloaded from https://advanced.onlinelibrary.wiley.com/doi/10.1002/adfm.202510233 by University Of North Carolina, Wiley Online Library on [22/07/2025]. See the Terms and Conditions (https://onlinelibrary.wiley.com/terms-and-conditions) on Wiley Online Library for rules of use; OA articles are governed by the applicable Creative Commons License

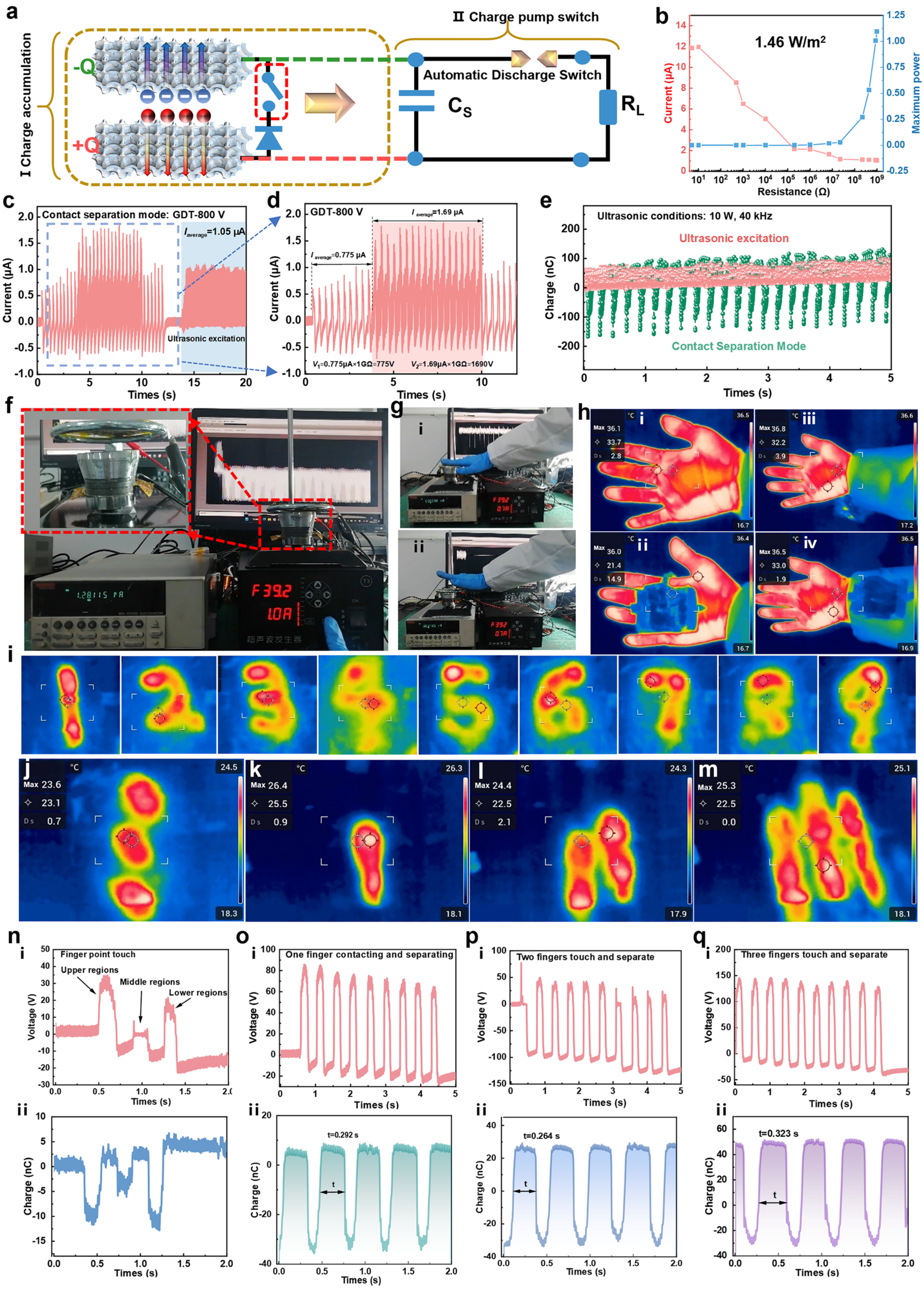

Figure 5. a) Equivalent circuit diagram of the room-temperature LMs generator. b) Power curve in ultrasonic mode. c) The output current and d) amplified signal when the 1 GΩ resistance load is coupled with the contact-separation mode and ultrasonic mode. e) Transfer of charge by ultrasound and contact-separation mode. f) Physical photos of ultrasonic generators and transducers. g) Photos before/after triggering the device by hand. h) Thermal imaging images when the device is wearable on the human body. i) Thermal imaging images of writing consecutive numbers with a finger. j–m) Thermal imaging distributions of the device triggered by different parts of the hand and n–q) Corresponding electrical signals.

© 2025 Wiley-VCH GmbH

16163028, 0, Downloaded from https://advanced.onlinelibrary.wiley.com/doi/10.1002/adfm.202510233 by University Of North Carolina, Wiley Online Library on [22/07/2025]. See the Terms and Conditions (https://onlinelibrary.wiley.com/terms-and-conditions) on Wiley Online Library for rules of use; OA articles are governed by the applicable Creative Commons License

4. Experimental Section

The Preparation of Room-Temperature GaInSnCu Metals: Ga, In, Sn, and Cu were procured from Shanghai Aladdin Corporation. First, Ga, In, and Sn metal particles were blended in a mass ratio of 67: 20.5:12.5, and thoroughly mixed for 10 min using a homogenizer. Subsequently, the mixture was heated to 100 °C under nitrogen protection and maintained for 12 h before being naturally cooled to obtain the $Ga_{67}In_{20.5}Sn_{12.5}$ alloy. Then, by controlling the mass ratio of GaInSn and Cu, the mixture was heated to 250 °C under nitrogen protection and held for 72 h before being naturally cooled, thereby attaining a GaInSnCu metal with a 5%, 10%, 15% mass fraction of Cu.

Preparation of Triboelectric Nanogenerator (TENG): Preparation of porous PTFE layer/LMs layer: The porous PTFE samples No. 01, 02, and 03 were respectively used as flexible substrates. After the surface was treated by plasma (50 W, 60 s, in an oxygen atmosphere), GaInSnCu metal was scraped and coated on the surfaces of the different porous PTFE layers using a stainless steel rod to form the embedded layer. Then, this surface was flipped to serve as the bottom (with an effective area of 2.5 cm × 2.5 cm) and connected through conductive silver cloth as the bottom electrode (positive output terminal). Conductive silver cloth (30 mm × 3 mm) was pasted on the upper surface of the porous PTFE layer as the top electrode (negative output terminal). Finally, polytetrafluoroethylene films with thicknesses of 0.05, 0.1, and 0.15 mm, respectively, were used as the encapsulation layer to prepare porous PTFE membranes of different thicknesses. Subsequently, the positive and negative output terminals of the corresponding devices were connected to obtain a TENG, which was connected to the load to form a circuit for testing the electrical properties.

Measurements and Characterizations: The Scanning Electron Microscopy (SEM) tests were conducted using a Zeiss Sigma300 system. Energy Spectrum Scanning (EDS) tests were performed with an Oxford Xplore30 system. The open circuit voltage (V_{oc}), short-circuit current (I_{sc}) and transfer charge (Q_{sc}) of TENG were characterized using an electrometer (Keithley 6514). The out-of-range voltage in this article was calculated based on the current through a 1GΩ load resistor connected in series with an electrometer. The mercury intrusion test was carried out with AUTOPORE 9600 of Micromeritics, USA. The thermal images were obtained by using the FLIR E8 Pro thermal imager of FLIR Systems, Inc., USA. High-speed photography images and videos were captured using industrial cameras (Dark Spectrum, NPX-GS6500UM, China). The tensile testing device was the SC-1000N from Shenzhen Shence Instrument Co., Ltd. in Shenzhen, China. The industrial ultrasonic generator was the THD-T3 from Shenzhen Taiheda Technology Co., Ltd. in Shenzhen, China. The human wearable data test has been approved by the Ethics Committee of the School of Energy and Environmental Sciences (No. 1), and all participants have signed the informed consent form.

Supporting Information

Supporting Information is available from the Wiley Online Library or from the author.

Acknowledgements

This work was funded by the National Natural Science Foundation of China Projects (62465019), Yunnan Province University Service Key Industry Science and Technology Projects (FWCY-ZNT2024008), Yunnan Revitalization Talent Support Program; Spring City Plan: the High-level Talent Promotion and Training Project of Kunming (2022SCP005). Yunnan Industrial Technology Innovation Reserve Talent Project (202105AD160056). Reserve Talents Project for Youth and Middle-Aged Academic and Technical Leaders of Yunnan Province (202205AC160032). Yunnan Fundamental Research Projects (202301AU070142, 202401AT070306, 202501AT070011, 202501AT070010), the PhD Starting Fund program of Yunnan Normal University (2021ZB005, 01100205020503225), Wisdom Yunnan Project (202403AM140035), Project for Building a Science and Technology Innovation Center Facing South Asia and Southeast Asia (202403AP140015). The authors thank the Electron Microscopy Center, the Advanced Analysis and Measurement Center of Yunnan University for the sample testing service.

Conflict of Interest

The authors declare no conflict of interest.

Data Availability Statement

The data that support the findings of this study are available from the corresponding author upon reasonable request.

Keywords

friction interface arrays, flexible wearable generators, hybrid energy harvesting, liquid metals, multiphase soft materials

Received: April 23, 2025
Revised: June 6, 2025
Published online:

---

[1] D. Wang, J. Ye, Y. Bai, F. Yang, J. Zhang, W. Rao, J. Liu, *Adv. Mater.* **2023**, *35*, 2303533.
[2] G. Li, M. Zhang, S. Liu, M. Yuan, J. Wu, M. Yu, L. Teng, Z. Xu, J. Guo, G. Li, Z. Liu, X. Ma, *Nat. Electron.* **2023**, *6*, 154.
[3] Y. He, J. You, M. D. Dickey, X. Wang, *Nat. Chem. Eng.* **2024**, *1*, 293.
[4] S. Chen, H. Wang, T.-Y. Liu, J. Liu, *Adv. Intell. Syst.* **2023**, *5*, 2309182.
[5] R. Yuan, Y. Cao, X. Zhu, X. Shan, B. Wang, H. Wang, S. Chen, J. Liu, *Adv. Mater.* **2023**, *36*, 202103142.
[6] H. Qin, L. Xu, S. Lin, F. Zhan, K. Dong, K. Han, H. Wang, Y. Feng, Zhong Lin Wang, *Adv. Funct. Mater.* **2022**, *32*, 2111662.
[7] X. Ye, Z. Zheng, J. G. Werner, John William Boley, *Adv. Funct. Mater.* **2023**, *34*, 2309177.
[8] H.-W. Zhou, C. Zhao, Z.-Y. Zhao, J.-C. Jiang, H.-L. Jin, S. Wang, S. Pan, M.-Y. Xu, Y.-H. Chen, H.-M. Jin, *Rare Met.* **2023**, *43*, 1186.
[9] F. Yin, H. Niu, Eun Seong Kim, Young Kee Shin, Y. Li, N.-Y. Kim, *InfoMat* **2023**, *5*, 12424.
[10] J. Dong, S. Huang, J. Luo, J. Zhao, F. R. Fan, Z.-Q. Tian, *Nano Energy* **2022**, *95*, 106971.
[11] J. Guo, X. Yang, Y. Xie, J. Zheng, W. Lin, J. Liao, H. Huang, J. Duan, P. Yang, Q. Tang, Z. L. Wang, *Device* **2024**, *3*, 100562.
[12] S. Zheng, X. Wang, W. Li, Z. Liu, Q. Li, F. Yan, *Nat. Electron.* **2024**, *7*, 576.
[13] S. Wang, Z. Ouyang, S. Geng, Y. Wang, X. Zhao, B. Yuan, X. Zhang, Q. Xu, C. Tang, S. Tang, H. Miao, H. Peng, H. Sun, *Natl. Sci. Rev.* **2024**, *11*, nwae006.
[14] K. Nan, S. Babaee, W. W. Chan, J. L. P. Kuosmanen, V. R. Feig, Y. Luo, S. S. Srinivasan, C. M. Patterson, A. M. Jebran, G. Traverso, *Nat. Biomed. Eng.* **2022**, *6*, 1092.
[15] J. Gao, J. Ye, H. Zhang, Z. Xing, X. Wang, J. Liu, *Matter* **2023**, *6*, 2870.
[16] L. Duan, Y. Zhang, J. Zhao, Q. Li, J. Zhang, J. He, J. Liu, Q. Liu, *ACS Appl. Electron. Mater.* **2022**, *4*, 112.
[17] H. Luo, L. Zhang, H. Yang, W. Yang, Q. Liu, W. Mu, Khampheng Boudmyxay, J. Liu, P. Yang, L. Duan, *Adv. Funct. Mater.* **2024**, *35*, 2413156.
[18] L. Zhao, X. Guo, Y. Pan, S. Jia, L. Liu, W. A. Daoud, P. Poechmueller, X. Yang, *InfoMat* **2024**, *6*, 12520.
[19] W. Xu, J. Guo, H. Wen, X. Meng, H. Hong, J. Yuan, J. Gao, D. Liu, Q. Ran, Y. Wang, J. Duan, Q. Tang, X. Yang, *Nano Energy* **2022**, *99*, 107348.

© 2025 Wiley-VCH GmbH

16163028, 0, Downloaded from https://advanced.onlinelibrary.wiley.com/doi/10.1002/adfm.202510233 by University Of North Carolina, Wiley Online Library on [22/07/2025]. See the Terms and Conditions (https://onlinelibrary.wiley.com/terms-and-conditions) on Wiley Online Library for rules of use; OA articles are governed by the applicable Creative Commons License

[20] J. Guo, L. Duan, W. Yang, Q. Wang, Y. Zhang, Y. Zhang, Z. L. Wang, P. Yang, *Nano Energy* **2024**, *131*, 110305.
[21] Z. Ma, Q. Huang, Q. Xu, Q. Zhuang, X. Zhao, Y. Yang, H. Qiu, Z. Yang, C. Wang, Y. Chai, Z. Zheng, *Nat. Mater.* **2021**, *20*, 859.
[22] C. Qin, D. Wang, Y. Liu, P. Yang, T. Xie, L. Huang, H. Zou, G. Li, Y. Wu, *Nat. Commun.* **2021**, *12*, 7184.
[23] X. Zhang, D. Ren, H. Wu, J. Wang, X. Li, H. Yang, Q. Li, Q. Yang, J. Zhu, Y. Xi, *Energy Environ. Sci.* **2024**, *17*, 4175.
[24] H. Wang, Y. Kurokawa, J. Wang, W. Cai, J. Zhang, S. Kato, Noritaka Usami, *Small* **2023**, *20*, 2308531.
[25] Q. Zhang, Y. Li, H. Cai, M. Yao, H. Zhang, L. Guo, Zhenjie Lv, M. Li, X. Lu, C. Ren, P. Zhang, Y. Zhang, X. Shi, G. Ding, J. Yao, Z. Yang, Zhong Lin Wang, *Adv. Mater.* **2021**, *33*, 2105761.
[26] H. Wu, Y. Kang, K. Li, J. Wang, S. Xu, G. Li, Q. Zhao, H. Yi, X. Pu, C. Hu, *ACS Energy Lett.* **2024**, *9*, 4516.
[27] X. Yan, W. Xu, Y. Deng, C. Zhang, H. Zheng, S. Yang, Y. Song, P. Li, X. Xu, Y. Hu, L. Zhang, Z. Yang, S. Wang, Z. Wang, *Sci. Adv.* **2022**, *8*, abo7698.
[28] A. Chen, Q. Zeng, L. Tan, T. Wang, F. Xu, J. Wang, X. Tao, Y. Yang, X. Wang, *Adv. Funct. Mater.* **2024**, *34*, 2405698.
[29] X. Li, S. Li, X. Guo, J. Shao, Z. L. Wang, D. Wei, *Matter* **2023**, *6*, 3912.
[30] X. Che, H. Yu, T. Wang, B. Zhang, Z. Zhai, Y. Chen, D. Pei, M. Li, C. Li, *Adv. Funct. Mater.* **2024**, *35*, 2415323.
[31] King Yan Chung, B. Xu, D. Tan, Q. Yang, Z. Li, H. Fu, *Nano-Micro Lett.* **2024**, *16*, 149.
[32] H.-W. Zhou, C. Zhao, Z.-Y. Zhao, J.-C. Jiang, H.-L. Jin, S. Wang, S. Pan, M.-Y. Xu, Y.-H. Chen, H.-M. Jin, *Rare Metals* **2023**, *43*, 1186.
[33] C. Fu, W. Tang, Y. Miao, A. Xu, Azadeh Nilghaz, W. Xu, K. Dong, B. Su, Z. Xia, *Nano Energy* **2023**, *106*, 108078.
[34] J. Yang, J. Cao, J. Han, Y. Xiong, L. Luo, X. Dan, Y. Yang, L. Li, J. Sun, Q. Sun, *Nano Energy* **2022**, *101*, 107582.
[35] X. Qi, Y. Liu, L. Yu, Z. Yu, L. Chen, X. Li, Y. Xia, *Adv. Sci.* **2023**, *10*, 2303406.
[36] Z. Li, B. Xu, J. Han, D. Tan, J. Huang, Y. Gao, H. Fu, *Chem. Eng. J.* **2023**, *460*, 141737.
[37] Y. Wang, C. Zhao, L. Chen, Q. Wu, Z. Zhao, Jing-Jing Lv, S. Wang, S. Pan, M. Xu, Y. Chen, H. Jin, *Nano Energy* **2024**, *127*, 109808.
[38] S. Li, Z. Zhang, F. Yang, X. Li, P. Peng, Y. Du, Q. Zeng, M. Willatzen, Z. L. Wang, D. Wei, *Device* **2024**, *2*, 100332.
[39] X. Li, R. Li, S. Li, Z. L. Wang, D. Wei, *Nat. Commun.* **2024**, *15*, 6182.
[40] F. Zhan, A. C. Wang, L. Xu, S. Lin, J. Shao, X. Chen, Zhong Lin Wang, *ACS Nano* **2020**, *14*, 17565.
[41] W. Lee, H. Kim, I. Kang, H. Park, J. Jung, H. Lee, H. Park, Ji Su Park, Jong Min Yuk, S. Ryu, J.-W. Jeong, J. Kang, *Science* **2022**, *378*, 637.
[42] Y. He, Z. Zhao, Y. Cui, W. Shang, Y. Chen, P. Tan, *Energy Storage Mater.* **2023**, *57*, 360.
[43] J. Dong, L. Zhu, P. Guo, C. Xu, X. Zhao, S. Yang, X. He, G. Zhou, G. Ma, H. Guo, C. Hu, Q. Song, *Energy Environ. Sci.* **2023**, *16*, 1071.
[44] R. Hinchet, H.-J. Yoon, H. Ryu, M.-K. Kim, E.-K. Choi, D.-S. Kim, S.-W. Kim, *Science* **2019**, *365*, 491.
[45] B. Kim, H.-J. Yoon, Y.-J. Kim, B.-J. Park, J.-H. Jung, S.-W. Kim, *ACS Energy Lett.* **2023**, *8*, 3412.
[46] W. Zhang, P.-L. Wang, L.-Z. Huang, W.-Y. Guo, J. Zhao, M.-G. Ma, *Nano Energy* **2023**, *117*, 108875.
[47] Y. Yang, N. Sun, Z. Wen, P. Cheng, H. Zheng, H. Shao, Y. Xia, C. Chen, H. Lan, X. Xie, C. Zhou, J. Zhong, X. Sun, S.-T. Lee, *ACS Nano* **2018**, *12*, 2027.
[48] Y. Zhang, H. Zhu, S. An, W. Xing, B. Fu, P. Tao, W. Shang, J. Wu, M. D. Dickey, C. Song, T. Deng, *Nat. Commun.* **2024**, *15*, 5395.
[49] X. Zhou, P. Min, Y. Liu, M. Jin, Z.-Z. Yu, H.-B. Zhang, *Science* **2024**, *385*, 1205.
[50] H. Wang, B. Yuan, X. Zhu, X. Shan, S. Chen, W. Ding, Y. Cao, K. Dong, X. Zhang, R. Guo, Y. Yao, B. Wang, J. Tang, J. Liu, *Sci. Adv.* **2024**, *10*, 21.
[51] B. Li, Y. Yang, J. Chen, J. Shen, X. Liu, Y. Lu, L. Ji, Z. Yang, J. Cheng, *Nano Energy* **2023**, *108*, 108200.
[52] A. Ghaffarinejad, J. Y. Hasani, R. Hinchet, Y. Lu, H. Zhang, A. Karami, D. Galayko, S.-W. Kim, P. Basset, *Nano Energy* **2018**, *51*, 173.
[53] Z. Yang, F. Liu, B. Li, Y. Li, X. Liu, J. Chen, C. Wang, L. Ji, Y. Yang, Zhong Lin Wang, J. Cheng, *Nano Energy* **2022**, *98*, 107264.

16163028, 0, Downloaded from https://advanced.onlinelibrary.wiley.com/doi/10.1002/adfm.202510233 by University Of North Carolina, Wiley Online Library on [22/07/2025]. See the Terms and Conditions (https://onlinelibrary.wiley.com/terms-and-conditions) on Wiley Online Library for rules of use; OA articles are governed by the applicable Creative Commons License